

Infrared Metasurface Augmented by Deep Learning for Monitoring Dynamics between All Major Classes of Biomolecules

Aurelian John-Herpin, Deepthy Kavungal, Lea von Mücke, and Hatice Altug*

Insights into the fascinating molecular world of biological processes are crucial for understanding diseases, developing diagnostics, and effective therapeutics. These processes are complex as they involve interactions between four major classes of biomolecules, i.e., proteins, nucleic acids, carbohydrates, and lipids, which makes it important to be able to discriminate between all these different biomolecular species. In this work, a deep learning-augmented, chemically-specific nanoplasmonic technique that enables such a feat in a label-free manner to not disrupt native processes is presented. The method uses a highly sensitive multiresonant plasmonic metasurface in a microfluidic device, which enhances infrared absorption across a broadband mid-IR spectrum and in water, despite its strongly overlapping absorption bands. The real-time format of the optofluidic method enables the collection of a vast amount of spectrotemporal data, which allows the construction of a deep neural network to discriminate accurately between all major classes of biomolecules. The capabilities of the new method are demonstrated by monitoring of a multistep bioassay containing sucrose- and nucleotides-loaded liposomes interacting with a small, lipid membrane-perforating peptide. It is envisioned that the presented technology will impact the fields of biology, bioanalytics, and pharmacology from fundamental research and disease diagnostics to drug development.

The ability to detect and monitor biomolecules is essential to extend our understanding of biological processes of both physiological and pathological order. Biosensors enabling the analysis of biomolecules from a wide range of samples are indispensable tools for analytical and biochemical studies as well as for medical diagnostics, safety, and industrial applica-

tions. In this regard, plasmonic biosensors employing nanoparticles and localized surface plasmon resonances (LSPR) have been receiving significant attention over the years due to their advantages, including high sensitivity and label-free operation.^[1] By detecting trace amounts of molecular compounds from minute samples, their use has been shown in various settings including for diagnostics,^[2,3] environmental monitoring,^[4] food industry,^[5] and consumer products.^[6] Access to kinetic information at the monolayer level has also been demonstrated with applications in bioanalytics and pharmacology.^[7,8] The vast majority of LSPR sensors rely on refractive index change detection, and despite their advantage of high sensitivity, the method is inherently nonspecific and unable to identify the nature of the matter causing the refractive index shift. In order to achieve specificity with selective binding of the targeted analytes, LSPR sensors require biofunctionalization through surface chemistry. However, going beyond the detection of one or two target analytes is very chal-

lenging, especially for processes in which the net refractive index remains mostly unchanged due to simultaneously occurring association, dissociation, and removal events, making it difficult to perform accurate measurements and decouple the contribution of the individual analytes from the overall signal.^[9] This is where plasmonic biosensors tailored for optical spectroscopy bring unique advantages because nanoantenna sensors can be tuned so that their resonances spectrally match molecular vibrations of analytes of interest, thereby making chemically specific detection possible.^[10,11] While surface-enhanced Raman spectroscopy allows the detection of single molecules due to its extremely tight near-field confinement on the surface (with a decay length of a few nanometers only),^[12] surface-enhanced infrared absorption spectroscopy (SEIRAS) nanosensors have a biologically relevant sensing depth (several tens of nanometers), which make it possible to monitor larger entities, such as lipid vesicles interacting with various other biomolecules.^[13] These types of biological samples play a pivotal role in numerous physiological and biomedical studies, e.g., in the investigation of exosomes carrying proteins and nucleic acids used for intercellular communication or the

A. John-Herpin, D. Kavungal, L. von Mücke, Prof. H. Altug
 Institute of Bioengineering
 École Polytechnique Fédérale de Lausanne (EPFL)
 Lausanne 1015, Switzerland
 E-mail: hatice.altug@epfl.ch



The ORCID identification number(s) for the author(s) of this article can be found under <https://doi.org/10.1002/adma.202006054>.

© 2021 The Authors. Advanced Materials published by Wiley-VCH GmbH. This is an open access article under the terms of the Creative Commons Attribution-NonCommercial-NoDerivs License, which permits use and distribution in any medium, provided the original work is properly cited, the use is non-commercial and no modifications or adaptations are made.

DOI: 10.1002/adma.202006054

characterization of liposomes loaded with drugs such as siRNA to treat pathological conditions.^[14,15] SEIRAS using engineered nanoantennas is the ideal candidate for such studies; however, this research field is still in its infancy and several challenges remain to be addressed before a more widespread use can emerge. So far, most of the SEIRAS sensors exhibit narrowband resonances, thereby strongly restricting the number of absorption bands and analytes that can be analyzed. Many of these sensors have been tuned for protein detection via their characteristic Amide I and II absorption bands,^[16–20] with some even operating in water and providing information about their 3D structures.^[21–24] Given the importance of proteins in physiology and the challenge of their detection with IR spectroscopy due to the overlap between water and Amide absorption bands, such SEIRAS sensors represent an important milestone. The next challenge is to simultaneously detect different classes of biomolecules, which is complicated due to the broadband nature of IR spectroscopy. For instance, while the Amide I and II bands of proteins absorb around 6 μm , lipids absorb more strongly near 3 μm and nucleic acids and carbohydrates around 10 μm ; this demands to have a wide spectral coverage over 7 μm . Multiresonant metasurfaces represent a promising approach to address this challenge by providing several resonances to target spectrally distant absorption bands.^[25–29] At the same time, the increased wealth of collected absorption signals and their partial overlap requires the use of chemometrics to effectively discriminate between analytes spectroscopically.^[30] Recently, multiple linear regression (MLR) was used to resolve protein–lipid interactions in processes involving lipid vesicles with dual-resonant metasurfaces consisting of plasmonic nanorod antennas.^[9] While this approach showed promises, further developments are needed for simultaneous monitoring of a large number of analytes from all four major biomolecular classes without erroneous signal attributions by the readout system.

In this work, we experimentally demonstrate that deep learning empowers broadband plasmonic metasurfaces for SEIRAS by enabling the study of a multianalyte bioparticle system in water and in real-time. The biosample consists of liposome nanoparticles loaded with both sucrose and nucleotides, and upon their binding on the surface of the SEIRAS sensor integrated with microfluidics, we introduce melittin, a small cytolytic peptide, which perforates the lipid membranes of the liposomes. This interaction leads to the breakage of liposomes and dual cargo release as well as the formation of supported lipid bilayer (SLB) patches on the sensor. With our optofluidic biosensor we can resolve in real-time these interaction events between all four major classes of biomolecules without using any external labels. This feat is achieved by engineering a highly sensitive multiresonant metasurface providing large signal enhancements across a broad mid-IR spectrum ranging from below 1000 to above 3000 cm^{-1} to cover all the major absorption bands of biomolecules. Significantly, the signals from the broadband metasurface is extracted with a deep neural network (DNN) for effective and reliable discrimination between all the simultaneously present biomolecules. By introducing for the first time a deep learning approach to real-time in situ SEIRAS measurements with nanoantennas, we expand the capabilities to new horizons where experiment complexity and training data wealth go hand in hand. Augmenting

SEIRAS with deep learning unleashes a vast potential to tap into and provides a powerful tool for unraveling open questions in biology, such the role of exosomes in health and disease.

To perform in situ SEIRAS, we nanofabricate gold antenna arrays on a transparent calcium difluoride substrate (Figure 1a) and integrate the plasmonic chip in a polydimethylsiloxane (PDMS) microfluidic device so that the incident light comes from the backside of the chip and reflects back to the objective above (Figure 1b). In this way, less IR light gets lost due to absorption by water and the analytes flowing through the microfluidic device can be sensed via the evanescent electric fields emanating from the resonant nanoantennas (Figure 1c). The nanoantennas are tuned so as to provide three resonances (Figure 1d, black and gray curves) which overlap with the molecular vibrations of all the major biological building blocks, i.e., polypeptides, nucleic acids/nucleotides, lipids, and polysaccharides (Figure 1d, colored curves). In the experimentally measured reflectance (Figure 1d, dotted gray curve), in addition to the three resonance peaks of the nanoantennas, we observe two large reflectance dips caused by the absorption due to water molecule vibrations around 1650 and 3500 cm^{-1} . The numerical simulation (Figure 1d, solid black curve) does not feature these water absorption-caused modulations, as the imaginary part of water was not taken into account ($k_{\text{water}} = 0$) to visualize better the antenna resonances. The low-frequency antenna resonance around 1200 cm^{-1} is suitable to sense the strong asymmetric phosphate group stretching vibrations from nucleic acids ($\approx 1230 \text{ cm}^{-1}$) as well the characteristic stretching motion of the CO bond within the glycosidic linkage of carbohydrates ($\approx 1142 \text{ cm}^{-1}$),^[31,32] while the other two resonances around 1600 and 2900 cm^{-1} are tuned to sense the Amide I-II vibrations of proteins ($\approx 1650, \approx 1550 \text{ cm}^{-1}$) and methylene stretching vibrations of lipids ($\approx 2850, \approx 2920 \text{ cm}^{-1}$), respectively.^[9]

Our nanoplasmonic metasurface is a multiresonant grating order-coupled nanogap (MR-GONG) design based on the recently introduced grating order-coupled nanogap (GONG) antenna arrays.^[23] It combines a single resonant array (SR-GONG) with a novel dual resonant array (DR-GONG). Each biochip (Figure 1a) contains pairs of $250 \times 250 \mu\text{m}^2$ SR- and DR-GONG arrays separated by $100 \mu\text{m}^2$, which as a whole define a MR-GONG metasurface sensor (Figure 2a). In order to spectrally target four different major classes at the same time, we design the three resonances of the metasurface to be at 1200, 1600, and 2900 cm^{-1} by tuning the geometrical parameters of the two types of arrays as seen in Figure 2b.

The experimentally measured reflectance spectra from SR-, DR-, and MR-GONG in water match well with the numerical simulations (Figure 2c). Here, the imaginary part of the refractive index for water has been used in the simulation to take into account absorption by water. The positions of the grating orders were tuned by the y -periodicities of the arrays to boost the electric near field enhancements around the 1200, 1600, and 2900 cm^{-1} resonances (Figure 2d). The maximum near-field intensity enhancement in water surpasses 50 000 for the lower frequency resonance and scales with the third power of the wavelength for the two higher frequency resonances, in accordance with classical antenna theory.^[33] The grating order presence can be observed as small modulations in the

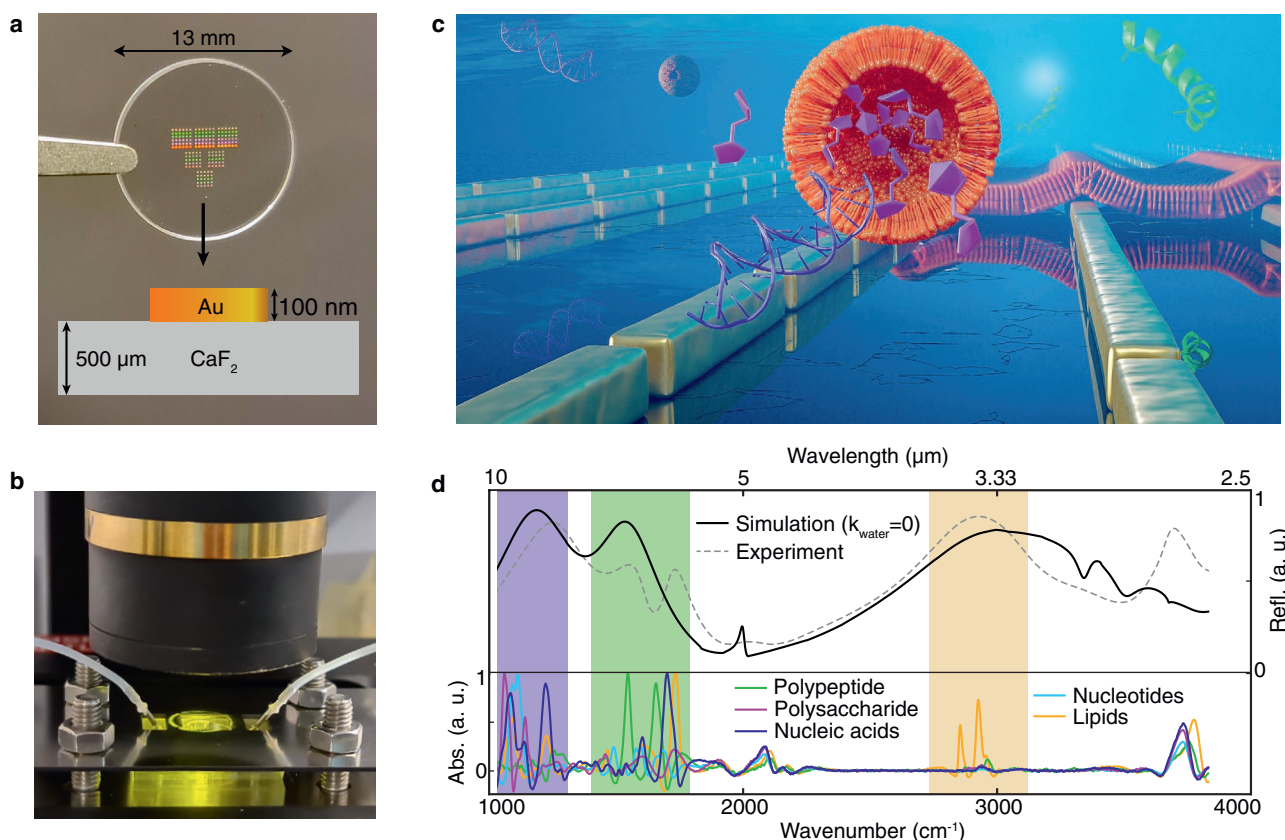


Figure 1. a) Top: Top-view picture of a representative plasmonic chip. Bottom: Side view schematic. b) Fluidic setup used for in situ micro-FTIR bio-experiments in water. A plasmonic chip is integrated into a PDMS device clamped below the micro-FTIR objective. c) Artwork showcasing the flow over plasmonic antennas of polypeptides, nucleic acids, lipid vesicles, and polysaccharides. d) Plot displaying the metasurface's numerically simulated (black solid curve) as well as experimentally measured reflectance spectrum in water (gray dotted curve) together with the absorption spectra of five species from all the major classes of biomolecules (colored curves). In the simulation, the imaginary part of water was not taken into account ($k_{\text{water}} = 0$) to visualize better the antenna resonances, which are highlighted with colored, shaded areas.

reflectance spectra at multiple locations, and the most prominent ones are around 2000 and 3800 cm⁻¹.

Next, we experimentally demonstrate the applicability of the metasurface with a dynamically interacting nanoparticle biosystem (Figure 1c), which features multiple different species, including melittin polypeptides and lipid vesicles loaded with nucleotides as well as sucrose polysaccharides. Successfully resolving the interactions between all these analytes in water medium would open the door to studies with native vesicles, such as exosomes or biomedical liposomes loaded with drugs. To perform real-time in situ SEIRAS measurements, we continuously measure the reflectance spectrum R of the MR-GONG metasurface and compute the absorbance with respect to the initial baseline spectrum R_0 as $-10^3 \cdot \log_{10}(R/R_0)$. The thereby obtained real-time absorbance spectra incorporate the IR signatures of the four analytes (Figure 3a). The grayscale color bar in Figure 3a represents discrete time points, and the complete spectrotemporal data can be seen in Figure 4d as a 3D plot. To identify the contributions of each analyte at different time points, we have initially tested the use of MLR to model the relationship between the overall real-time

absorbance signal and the individual analyte absorbance signal contributions by least-squares fitting.

SEIRAS spectra typically appear on a skewed baseline (Figure 3a) as a consequence of spectral shifting of the antenna resonance wavelengths throughout the experiment, which is due to the effective refractive index change in the antenna vicinity as analytes are introduced. We take this effect into account in the preprocessing of the raw spectra where we subtract an asymmetric least squares (ALS) fit to have the real-time absorbance signals centered around zero (Figure 3b). To implement MLR, the resulting spectra (Figure 3b) and the reference absorbance spectra of all the analytes present in the experiment (Figure 3c) are fed into the model to extract the regression coefficients for each analyte and time point (Figure 3d). Most of the substantial absorbance changes (Figure 3a,b) happen within the first hour after baseline, i.e., between 30 and 90 min (Figure 3d) and the rest of the experiment features only subtle spectral changes over a longer time window, i.e., from 100 to 320 min. As shown in Figure 3e, we start the assay with a plasmonic chip functionalized with biotinylated thiols to which biotinylated vesicle tethers are bound via an intercalated streptavidin layer, which corresponds to the initial stable baseline in Figure 3d. Half an hour

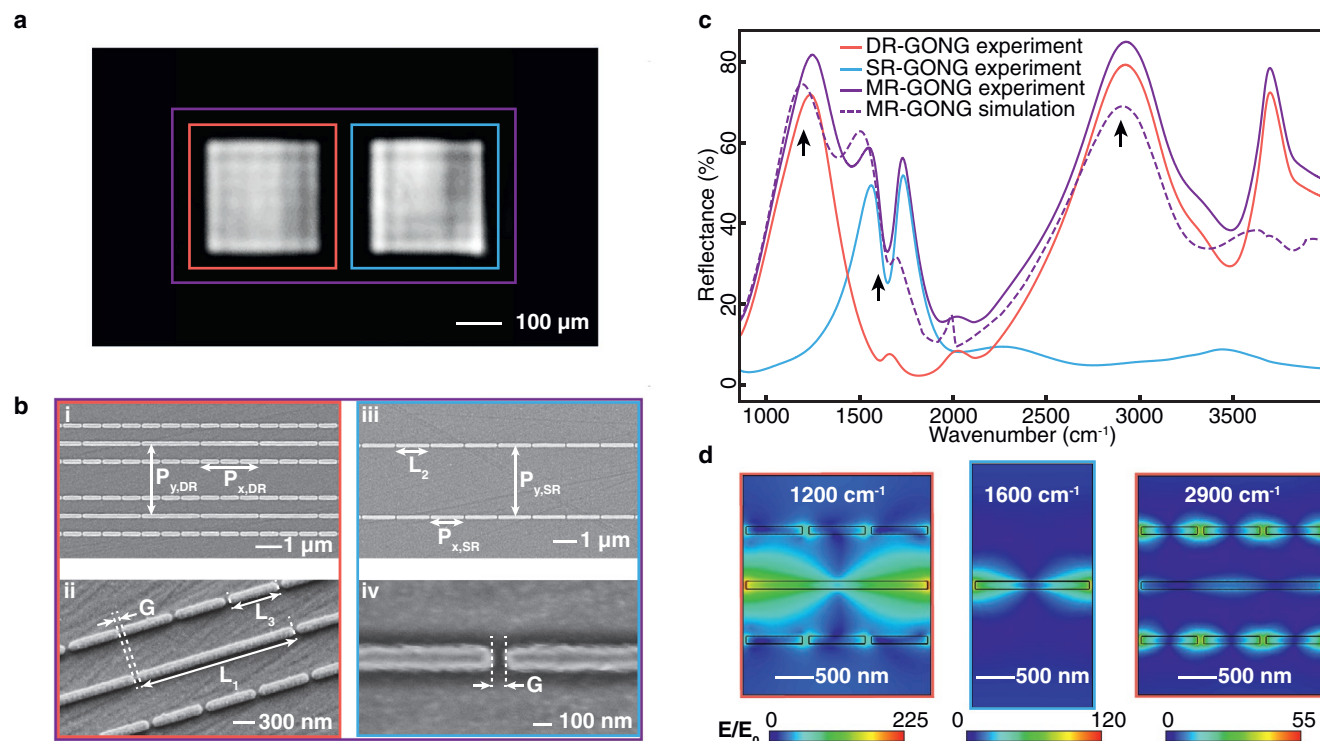


Figure 2. a) Infrared reflectance microscopy image in dry conditions obtained using quantum cascade laser light at 6 μm wavelength. Two 250 × 250 μm² arrays can be seen with red and blue squares identifying DR- and SR-GONG arrays, respectively. Together, the two arrays form the MR-GONG metasurface indicated with the purple rectangle. b) Scanning electron microscopy (SEM) images of: i) a DR-GONG array with periodicities $P_{x,DR} = 2.4 \mu\text{m}$ and $P_{y,DR} = 2.9 \mu\text{m}$, and ii) antenna lengths $L_1 = 2.32 \mu\text{m}$ and $L_3 = 0.72 \mu\text{m}$ as well as interantenna gap size $G = 80 \text{ nm}$, iii) an SR-GONG array with periodicities $P_{x,SR} = 1.58 \mu\text{m}$, $P_{y,SR} = 3.2 \mu\text{m}$ and antenna length $L_2 = 1.5 \mu\text{m}$, and iv) an interantenna gap size $G = 80 \text{ nm}$. c) Micro-FTIR measured SR- and DR-GONG arrays in water as well as the combined MR-GONG metasurface reflectance, incl. numerically simulated spectrum. The arrows indicate the spectral positions at which we show d) numerically simulated electric field enhancements around the three resonances in water.

after the start of the experiment, the lipid, sucrose, and nucleotide signals start to rise, as can be seen in the tricolor shaded area of Figure 3d. This corresponds to the injection and capturing of liposomes filled and surrounded with nucleotides and sucrose, as is depicted in Figure 3e. Interestingly, this injection also induces a negative melittin curve, although the peptide is only introduced later in the experiment; we will discuss this point later in the text. The liposome capture is followed by the rinsing of the surface with the buffer solution (white shaded areas in Figure 3d), leading to the stabilization of the signals at $t = 100 \text{ min}$. Specifically, the lipid signal reaches a stable maximum, while the sucrose and nucleotide signals peak before stabilizing above zero. This can be understood with the help of Figure 3e schematics, i.e., the loaded liposomes are captured by the surface-displayed tethers, while the extravesicular nucleotide and sucrose molecules gradually rinse off with the flowing buffer. The remaining nucleotide and sucrose signals correspond to the molecules trapped as liposome cargo on the antenna surfaces.

An hour after all the signals have stabilized, we perform the first injection of $3 \times 10^{-6} \text{ M}$ cytolytic polypeptide melittin, which results in a slight increase of the melittin curve while the curves of the other analytes remain largely unaffected. It appears that at this concentration melittin binds without forming pores in the membranes^[34] composed of 40 mol% 1-palmitoyl-2-oleoyl-sn-glycero-3-phosphocholine (POPC), 20 mol% 1,2-dioleoyl-

sn-glycero-3-phosphoethanolamine (DOPE), 20 mol% 1-palmitoyl-2-oleoyl-sn-glycero-3-phospho-L-serine (POPS), and 20 mol% cholesterol. For the second injection at $t = 220 \text{ min}$, we increase the melittin concentration to $6 \times 10^{-6} \text{ M}$. At this higher concentration the peptides should breach the lipid membranes and thereby lead to the release of nucleotides and sucrose.^[35] However, this is not observed in the MLR sensorgrams, which points toward the limitations of the analysis. Another artefact of the MLR analysis is that before the peptide is even introduced on the sensor, the melittin curve becomes negative after the nanoparticle injection and remains below zero throughout the experiment. We believe that this artefact is mostly caused by the displaced water molecules from the binding of the nanoparticles on the sensors' surface and the overlapping water absorption band with the Amide I band of polypeptides. In addition to the water interference, another complication for the MLR analysis arises from erroneous absorption signals caused by the grating order positions shifting with the change in the effective refractive index within the vicinity of the antennas throughout the experiment. This effect can be clearly visualized in Figure 3c, where we detect signal that resembles absorption bands in a spectral window (2000–2200 cm⁻¹), which should normally be transparent. In fact, the origin of this signal can be traced back to the grating orders in that range because their corresponding peaks are observable in the resonance spectrum

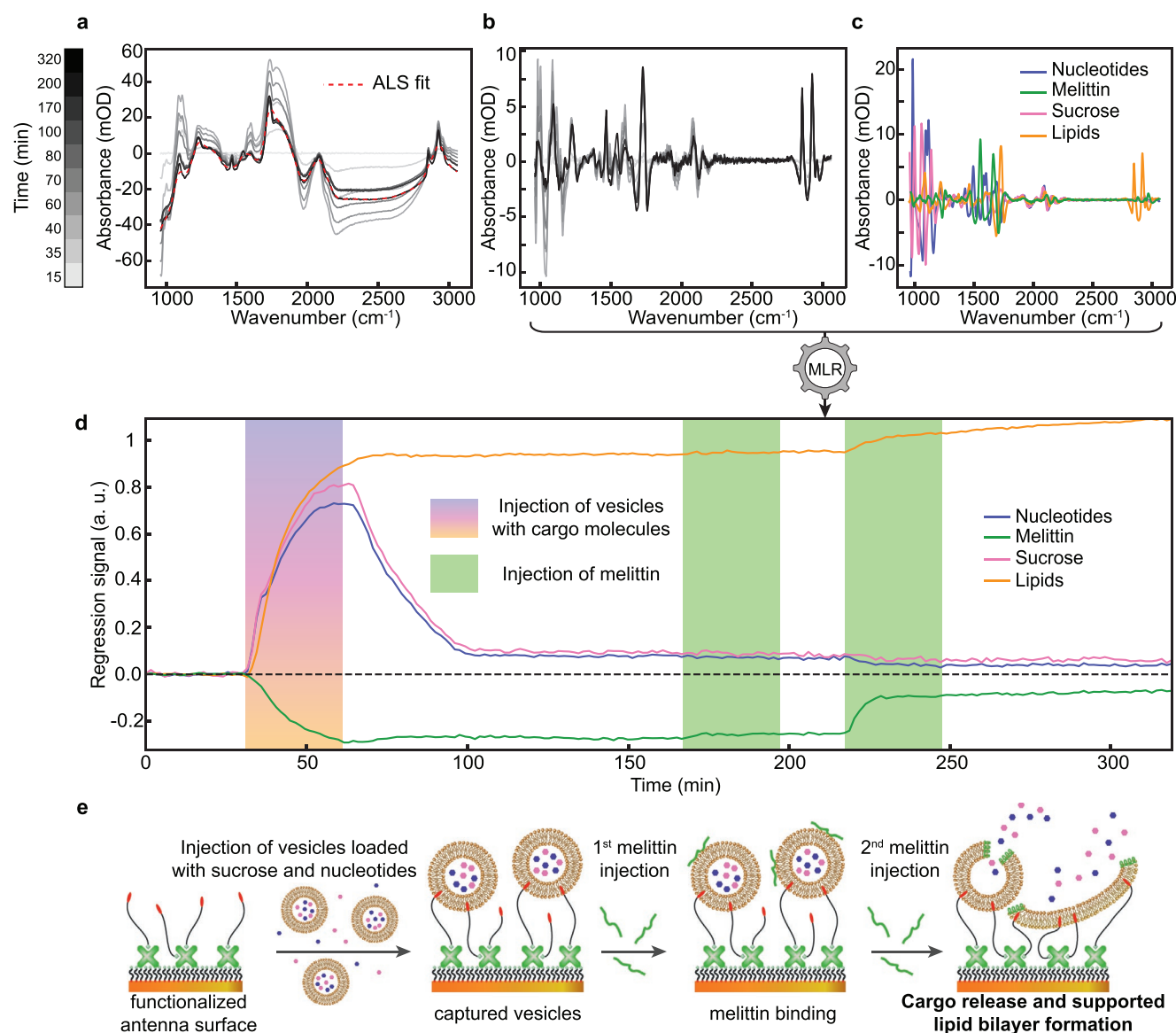


Figure 3. a) Real-time absorbance spectra calculated as $-10^3 \log_{10}(R/R_0)$ with R the reflectance spectrum of the MR-GONG metasurface and R_0 the baseline reflectance. The asymmetric least squares (ALS) fit for the ultimate spectrum is also shown. The grayscale bar represents discrete time points. b) Absorbance spectra after subtracting the ALS fit for each spectrum. c) Reference absorption spectra for the four bioanalytes used to apply multiple linear regression (MLR) to obtain d) the regression curves of the dynamic experiment involving lipid vesicles, sucrose, nucleotides, and melittin. e) Schematic depiction of the experiment.

of the metasurface (Figures 1d and 2c). Overall, even though the spectral signatures extracted by MLR give some insights into the molecular events happening on the metasurface, it is evident that MLR is not performing accurately. In fact in comparison to our earlier work with fewer numbers of analytes (i.e., three excluding the water medium),^[9] we encounter that MLR is rather simplistic to fully resolve the signals over a broader spectrum when there are more analytes present in the sample simultaneously.

To address these shortcomings, we develop a DNN to discriminate between different molecular components effectively. In general, deep learning models require a large set of input

data to work accurately,^[36–38] this is in stark contrast to the MLR approach, which only needed one spectrum per analyte for the input references. These single spectrum references (Figure 3c) were extracted from additional real-time measurements featuring only one analyte at a time. These measurements can be seen in Figure 4a, where we performed three real-time in situ experiments, i.e., one with melittin, one with nucleotides as well as sucrose, and one with empty lipid vesicles. In the first experiment, we flow melittin onto the bare sensing surface while continuously measuring the spectra to obtain a 3D plot of absorbance for each spectral and temporal point. Next, we extract a single spectrum around the time of maximum signal,

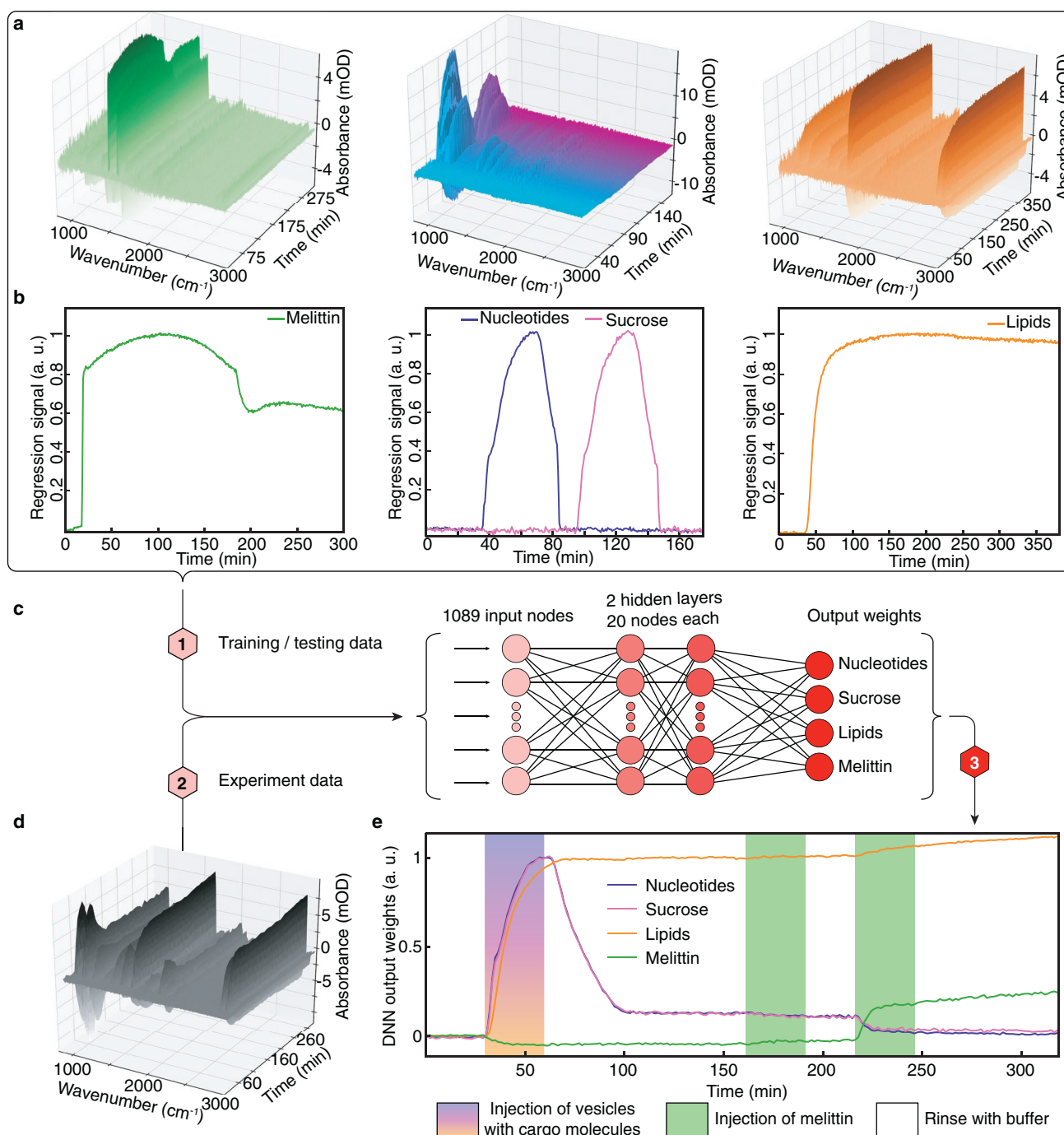


Figure 4. a) From several real-time measurements featuring melittin, nucleotides, sucrose, and lipids, the real-time 3D plots of absorbance signal versus time and wavenumber are extracted, b) as well as the associated regression curves obtained by MLR. c) The absorbance plots together with the associated regression coefficients shown in (a,b) are then used to fit the deep neural network. d) The spectrotemporal data points of the dual cargo release experiment were subsequently fed into the trained network to e) predict the scaled DNN output weight curves for each analyte.

which we then use as a reference spectrum to get regression coefficients (Figure 4b). For the nucleotides and sucrose, we flow the molecules sequentially onto the sensor in a single experiment, as it is visible that these completely rinse off the functionalized surface (Figure 4b). Given the real-time format of these measurements, more spectral data are available than

the one that is used for the MLR analysis. We utilize all these spectra (Figure 4a) as well as their associated regression coefficients (Figure 4b) as input to build the DNN. Beyond the data shown in Figure 4a,b, we record a total input data set of more than three million spectrotemporal data points, from measurements featuring up to three analytes simultaneously

(Figure S1a,b, Supporting Information), which we use to fit our DNN. The DNN input layer has 1089 nodes to match the wave-number points of our spectra that spans from 960 to 3060 cm^{-1} with a 4 cm^{-1} resolution, and the output layer has four nodes to match the number of analytes (Figure 4c). After training/validating the DNN, we input the data of the experiment with the four analytes (Figure 4d) to predict the output weights for each analyte and time point (Figure 4e).

In Figure 4e, we observe the increase of lipid, sucrose, and nucleotide signals after half an hour of baseline as the liposomes and cargo/extravesicular molecules are injected onto the metasurface. At the end of the injection, the lipid signal stabilizes as the liposomes are captured on the surface, while the sucrose and nucleotide molecule signals initially drop as the buffer rinses the molecules off and then stabilize at $t = 100$ min, corresponding to the signal from the trapped cargo molecules only. In contrast with Figure 3d, the melittin signal barely features erroneous negative values and remains stable around zero before we introduce it onto the surface. Furthermore, as compared to Figure 3d, we can see a clear drop in the cargo molecule signals with the second melittin injection, evidencing the content release from the breached liposome membranes. As could already be seen previously in Figure 3d, this second melittin injection also leads to a pronounced increase in the lipid curve, which can be understood as the opening of some of the liposomes to form patches of SLBs in closer proximity to the sensing surfaces and thus giving stronger signals (Figure S3, Supporting Information). This effectively demonstrates the suitability of SEIRAS for sensing small molecules simultaneously with larger structures, such as lipid assemblies, as the antennas' evanescent fields can probe tens of nanometers away from the surface, thereby giving additional information regarding the analyte distribution along the surface normal. It is also important to highlight that the DNN approach helped to effectively reduce the interfering effects of grating orders and water displacement. These results show that the information extracted by the DNN yields superior performance in comparison to using only MLR.

In conclusion, we have introduced a deep learning-augmented infrared nanoplasmonic metasurface, which is broadly applicable to the study of biomolecular interactions. In addition to the high sensitivity, label-free, and chemical specificity characteristics of the spectroscopic biosensor, we also demonstrated its versatility and universality by simultaneously monitoring major biomolecule classes in water. Significantly, we could observe in real-time vesicle capture, perforation with dual cargo release, and partial transition to planar lipid bilayers. The biosensor offers numerous application prospects, including characterization of liposomal drugs,^[39,40] antimicrobial peptides,^[41,42] and exosomes.^[43,44] Besides biomolecular interactions involving lipid membranes, bioanalytical studies for the characterization of protein-DNA interactions in gene regulation,^[45] or protein-polysaccharide interactions in neurodegenerative diseases^[46,47] could also be investigated. The complexity of the tackled bioanalytical studies go hand in hand with the wealth of available DNN training data, which is both a blessing and a curse, as extensive data collection can be tedious but also brings the prospect of eventually unraveling the biomolecular events.^[48] Looking forward to future developments, one can envision the adaption of the technology to become compatible with mass-

production methods^[19,49–52] and miniaturization efforts^[53–56] for convenient diagnostics and therapeutics. This will probably require a move away from Au as the resonator material, and a Fourier-transform infrared (FTIR) spectroscope as the measurement instrument, because the former is not complementary metal-oxide-semiconductor (CMOS)-compatible and the latter is bulky and expensive. Among the alternatives to Au as the resonator material, CMOS-compatible materials such as Al and Si have shown promising results for SEIRAS via plasmonic and dielectric resonances, respectively.^[54,57] As for overcoming FTIR-related limitations, cutting edge measurement tools based on quantum cascade lasers and imaging-based microarrays offer the prospect of biosensor miniaturization.^[54,58,59]

Supporting Information

Supporting Information is available from the Wiley Online Library or from the author.

Acknowledgements

The research leading to these results has received funding from the European Research Council (ERC) under Grant Agreement No. 682167 (VIBRANT-BIO) and the European Union Horizon 2020 Framework Programme for Research and Innovation under Grant Agreement No. 777714 (NOCTURNO). The authors thank L. Joowon and B. Lavickova for useful discussions and acknowledge École Polytechnique Fédérale de Lausanne (EPFL) and Center of MicroNanoTechnology (CMI) for micro/nanofabrication.

Conflict of Interest

The authors declare no conflict of interest.

Keywords

biosensors, deep learning, infrared spectroscopy, metasurfaces, nanoplasmonics

Received: September 4, 2020

Revised: December 11, 2020

Published online: February 22, 2021

- [1] R. T. Hill, *Wiley Interdiscip. Rev.: Nanomed. Nanobiotechnol.* **2015**, 7, 152.
- [2] M. Soler, C. S. Huertas, L. M. Lechuga, *Expert Rev. Mol. Diagn.* **2019**, 19, 71.
- [3] A. Belushkin, F. Yesilkoy, J. J. González-López, J. C. Ruiz-Rodríguez, R. Ferrer, A. Fàbrega, H. Altug, *Small* **2020**, 16, 1906108.
- [4] C. Justino, A. Duarte, T. Rocha-Santos, *Sensors* **2017**, 17, 2918.
- [5] J.-F. Masson, *Analyst* **2020**, 145, 3776.
- [6] A. Polman, *Science* **2008**, 322, 868.
- [7] M. Couture, S. S. Zhao, J.-F. Masson, *Phys. Chem. Chem. Phys.* **2013**, 15, 11190.
- [8] S. G. Patching, *Biochim. Biophys. Acta, Biomembr.* **2014**, 1838, 43.
- [9] D. Rodrigo, A. Tittl, N. Ait-Bouziad, A. John-Herpin, O. Limaj, C. Kelly, D. Yoo, N. J. Wittenberg, S. Oh, H. A. Lashuel, H. Altug, *Nat. Commun.* **2018**, 9, 2160.

- [10] M. Tabatabaei, D. McRae, F. Lagugné-Labarthe, in *Frontiers of Plasmon Enhanced Spectroscopy*, Vol. 2, American Chemical Society, Washington, DC, USA **2016**, pp. 183–207.
- [11] L. Dong, X. Yang, C. Zhang, B. Cerjan, L. Zhou, M. L. Tseng, Y. Zhang, A. Alabastri, P. Nordlander, N. J. Halas, *Nano Lett.* **2017**, 17, 5768.
- [12] K. Kneipp, Y. Wang, H. Kneipp, L. T. Perelman, I. Itzkan, R. R. Dasari, M. S. Feld, *Phys. Rev. Lett.* **1997**, 78, 1667.
- [13] O. Limaj, D. Etezadi, N. J. Wittenberg, D. Rodrigo, D. Yoo, S. Oh, H. Altug, *Nano Lett.* **2016**, 16, 1502.
- [14] R. Kalluri, V. S. LeBleu, *Science* **2020**, 367, eaau6977.
- [15] L. M. Ickenstein, P. Garidel, *Expert Opin. Drug Delivery* **2019**, 16, 1205.
- [16] R. Adato, A. A. Yanik, J. J. Amsden, D. L. Kaplan, F. G. Omenetto, M. K. Hong, S. Erramilli, H. Altug, *Proc. Natl. Acad. Sci. USA* **2009**, 106, 19227.
- [17] K. Chen, T. D. Dao, S. Ishii, M. Aono, T. Nagao, *Adv. Funct. Mater.* **2015**, 25, 6637.
- [18] D. Rodrigo, O. Limaj, D. Janner, D. Etezadi, F. J. Garcia de Abajo, V. Pruneri, H. Altug, *Science* **2015**, 349, 165.
- [19] D. Yoo, D. A. Mohr, F. Vidal-Codina, A. John-Herpin, M. Jo, S. Kim, J. Matson, J. D. Caldwell, H. Jeon, N.-C. Nguyen, L. Martin-Moreno, J. Peraire, H. Altug, S.-H. Oh, *Nano Lett.* **2018**, 18, 1930.
- [20] M. Ye, K. B. Crozier, *Opt. Express* **2020**, 28, 18479.
- [21] E. Pfizner, H. Seki, R. Schlesinger, K. Ataka, J. Heberle, *ACS Sens.* **2018**, 3, 984.
- [22] D. Etezadi, J. B. Warner, H. A. Lashuel, H. Altug, *ACS Sens.* **2018**, 3, 1109.
- [23] A. John-Herpin, A. Tittl, H. Altug, *ACS Photonics* **2018**, 5, 4117.
- [24] R. Semenyshyn, F. Mörz, T. Steinle, M. Ubl, M. Hentschel, F. Neubrech, H. Giessen, *ACS Photonics* **2019**, 6, 2636.
- [25] K. Chen, R. Adato, H. Altug, *ACS Nano* **2012**, 6, 7998.
- [26] H. Aouani, H. Šípová, M. Rahmani, M. Navarro-Cia, K. Hegnerová, J. Homola, M. Hong, S. A. Maier, *ACS Nano* **2013**, 7, 669.
- [27] D. Rodrigo, A. Tittl, A. John-Herpin, O. Limaj, H. Altug, *ACS Photonics* **2018**, 5, 4903.
- [28] G. Q. Wallace, D. M. McRae, F. Lagugné-Labarthe, *Opt. Lett.* **2019**, 44, 3865.
- [29] G. Roubaud, P. Bondareff, G. Volpe, S. Gigan, S. Bidault, S. Grésillon, *Nano Lett.* **2020**, 20, 3291.
- [30] C. L. M. Morais, K. M. G. Lima, M. Singh, F. L. Martin, *Nat. Protoc.* **2020**, 15, 2143.
- [31] G. Socrates, *Infrared and Raman Characteristic Group Frequencies: Tables and Charts*, John Wiley & Sons, Chichester, UK **2001**.
- [32] E. Wiercigroch, E. Szafraniec, K. Czamara, M. Z. Pacia, K. Majzner, K. Kochan, A. Kaczor, M. Baranska, K. Malek, *Spectrochim. Acta, Part A* **2017**, 185, 317.
- [33] K. Weber, M. L. Nesterov, T. Weiss, M. Scherer, M. Hentschel, J. Vogt, C. Huck, W. Li, M. Dressel, H. Giessen, F. Neubrech, *ACS Photonics* **2017**, 4, 45.
- [34] G. van den Bogaart, J. V. Guzmán, J. T. Mika, B. Poolman, *J. Biol. Chem.* **2008**, 283, 33854.
- [35] M.-T. Lee, T.-L. Sun, W.-C. Hung, H. W. Huang, *Proc. Natl. Acad. Sci. USA* **2013**, 110, 14243.
- [36] S. Bigdeli, D. Honzátko, S. Süssstrunk, L. A. Dunbar, in *Proc. 15th Int. Joint Conf. Computer Vision, Imaging and Computer Graphics Theory and Applications - Volume 4: VISAPP*, Science and Technology Publications, Setúbal, Portugal **2020**.
- [37] C. Cao, F. Liu, H. Tan, D. Song, W. Shu, W. Li, Y. Zhou, X. Bo, Z. Xie, *Genomics, Proteomics Bioinf.* **2018**, 16, 17.
- [38] Z. S. Ballard, H.-A. Joung, A. Goncharov, J. Liang, K. Nugroho, D. Di Carlo, O. B. Garner, A. Ozcan, *npj Digital Med.* **2020**, 3, 66.
- [39] S. S. Knights-Mitchell, M. Romanowski, *Nanotheranostics* **2018**, 2, 295.
- [40] H. Rostamabadi, S. R. Falsafi, S. M. Jafari, *J. Controlled Release* **2019**, 298, 38.
- [41] É. Pardoux, A. Roux, R. Mathey, D. Boturyn, Y. Roupioz, *Talanta* **2019**, 203, 322.
- [42] É. Pardoux, D. Boturyn, Y. Roupioz, *Molecules* **2020**, 25, 1998.
- [43] M. Avella-Oliver, R. Puchades, S. Wachsmann-Hogiu, A. Maquieira, *Sens. Actuators, B* **2017**, 252, 657.
- [44] S. Zhu, H. Li, M. Yang, S. W. Pang, *Nanoscale* **2018**, 10, 19927.
- [45] Z. Swank, N. Laohakunakorn, S. J. Maerkl, *Science* **2019**, 116, 5892.
- [46] M. Goedert, R. Jakes, M. G. Spillantini, M. Hasegawa, M. J. Smith, R. A. Crowther, *Proc. Natl. Acad. Sci. USA* **1996**, 15, 15125.
- [47] Y. Wang, E. Mandelkow, *Nat. Rev. Neurosci.* **2015**, 17, 22.
- [48] A. Tittl, A. John-Herpin, A. Leitis, E. R. Arvelo, H. Altug, *Angew. Chem., Int. Ed.* **2019**, 58, 14810.
- [49] S. Aksu, A. A. Yanik, R. Adato, A. Artar, M. Huang, H. Altug, *Nano Lett.* **2010**, 10, 2511.
- [50] Z. Ding, J. M. Stubbs, D. McRae, J. M. Blacquiere, F. Lagugné-Labarthe, S. Mittler, *ACS Sens.* **2018**, 3, 334.
- [51] Y.-M. Bahk, D.-S. Kim, H.-R. Park, *Adv. Opt. Mater.* **2019**, 7, 1800426.
- [52] M. Bomers, B. Charlot, F. Barho, A. Chanuel, A. Mezy, L. Cerutti, F. Gonzalez-Posada, T. Taliércio, *React. Chem. Eng.* **2020**, 5, 124.
- [53] C. Chen, D. A. Mohr, H. K. Choi, D. Yoo, M. Li, S. H. Oh, *Nano Lett.* **2018**, 18, 7601.
- [54] A. Tittl, A. Leitis, M. Liu, F. Yesilkoy, D. Y. Choi, D. N. Neshev, Y. S. Kivshar, H. Altug, *Science* **2018**, 360, 1105.
- [55] A. Leitis, A. Tittl, M. Liu, B. H. Lee, M. B. Gu, Y. S. Kivshar, H. Altug, *Sci. Adv.* **2019**, 5, eaaw2871.
- [56] B. Cerjan, N. J. Halas, *ACS Photonics* **2019**, 6, 79.
- [57] M. W. Knight, L. Liu, Y. Wang, L. Brown, S. Mukherjee, N. S. King, H. O. Everitt, P. Nordlander, N. J. Halas, *Nano Lett.* **2012**, 12, 6000.
- [58] E. Tütüncü, B. Mizaikoff, *Anal. Bioanal. Chem.* **2019**, 411, 1679.
- [59] C. K. Akhgar, G. Ramer, M. Žbik, A. Trajnerowicz, J. Pawluczyk, A. Schwaighofer, B. Lendl, *Anal. Chem.* **2020**, 92, 9901.